

# Defective Nanoporous Zinc Cobaltite as a Potential Bifunctional Oxygen Electrocatalyst

Gowra Raghupathy Dillip,<sup>II</sup> Gundegowda Kalligowdanadoddi Kiran,<sup>II</sup> Abhishek Bharti, Tanmay Mohan Bhagwat, Gopalakrishnan Sai Gautam,<sup>\*</sup> and Aninda J. Bhattacharyya<sup>\*</sup>



Cite This: ACS Appl. Energy Mater. 2022, 5, 13635–13644



Read Online

ACCESS |

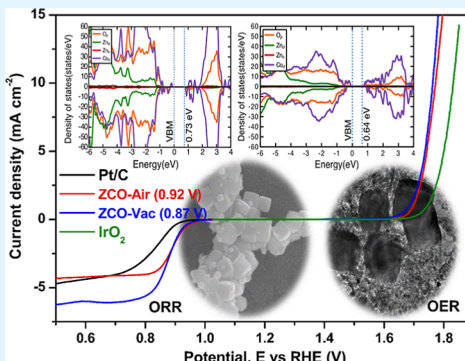
Metrics & More

Article Recommendations

Supporting Information

**ABSTRACT:** Efficient bifunctional oxygen catalyst is a crucial requirement to ensure optimal and stable performance in metal–air batteries and fuel cells, both of which are considered front runners to replace combustion technologies based on fossil fuels. Our work focuses on this critical requirement, and we propose, via a combined experiment-computation approach, a porous nanostructured non-stoichiometric zinc cobaltite ( $\text{ZnCo}_2\text{O}_4$ -ZCO) as an efficient bifunctional catalyst for oxygen reduction and evolution reactions (ORR and OER). The defects were incorporated into the ZCO nanocubes by sintering the product obtained from hydrothermal synthesis under different conditions. The ZCO samples annealed under air (ZCO-Air) and vacuum (ZCO-Vac) show bifunctional electrocatalytic activity (under alkaline conditions) toward ORR (@  $-3 \text{ mA cm}^{-2}$ ) and OER (@  $10 \text{ mA cm}^{-2}$ ) at potential differences of 0.92 and 0.87 V, respectively. Both samples exhibit superior electrocatalytic activity than the prevalent standards, namely, Pt/C for ORR and  $\text{IrO}_2$  for OER, and show long-term stability crucial for practical applications. As calculated using first principles, the electronic density of states confirms that defects formed during annealing of ZCO (in air/vacuum) play a crucial role in enhancing electrocatalytic activity by altering the band gap of bulk ZCO to more optimal levels, suitable for the oxygen electrocatalysis. With effective activity toward ORR and OER, the work here establishes ZCO, with an appropriate heat treatment protocol, to be a suitable bifunctional catalyst for metal–air batteries and fuel cells.

**KEYWORDS:** zinc cobaltite, non-stoichiometry, annealing atmosphere, electrocatalyst, density functional theory



## 1. INTRODUCTION

The overwhelming dependence on traditional fossil fuels has led to a significant global energy crisis. Consequently, there is a critical need to develop alternative renewable energy-based technologies which can substitute fossil fuels leading to a sustainable environment and living. Fuel cells, metal–air batteries, and water splitting devices<sup>1–3</sup> comprise a class of devices where the performance is predominantly determined by chemical processes such as the oxygen reduction reaction (ORR) and oxygen evolution reaction (OER).<sup>4–6</sup> Tian and co-workers discussed the advantages and limitations of ORR electrocatalysts, such as platinum group metal (PGM) catalysts, non-PGM catalysts, carbon-based, and single-atom-based catalysts.<sup>7</sup> Specifically, the ORR and OER are kinetically nontrivial, and there is a persistent demand for efficient oxygen electrocatalysts. Platinum (Pt)<sup>8</sup> and Pt-based materials<sup>9,10</sup> have been demonstrated as superior electrocatalysts for ORR. On the other hand,  $\text{RuO}_2$ <sup>11</sup> and  $\text{IrO}_2$ <sup>12</sup> are the best candidates for OER. However, these materials are not bifunctional, that is, they cannot be used simultaneously for ORR and OER. Additionally, they are expensive and scarcely abundant, thus limiting their practical usage. Therefore, it is essential to

develop efficient and cost-effective bifunctional oxygen electrocatalysts.

Several bifunctional catalysts have been proposed as alternatives to Pt-type metals. Wang et al., in their review article, outlined various composite materials with bifunctional activity for oxygen electrocatalysis.<sup>13</sup> Some of the candidate catalysts that have been studied include heteroatom-doped carbon materials,<sup>14–16</sup> transition-metal-based oxides, sulfides (such as  $\text{MnO}_2$ ,  $\text{Co}_3\text{O}_4$ ,  $\text{Co}_3\text{S}_4$ ,  $\text{Co}_9\text{S}_8$ , and  $\text{Ni}_3\text{S}_4$ ),<sup>17–20</sup> Ni-doped cobalt sulfides (such as  $\text{NiCo}_2\text{S}_4$ ,<sup>21</sup>  $\text{NiCo}_2\text{S}_4$ @graphene,<sup>22</sup> and  $\text{NiCo}_2\text{S}_4$ @g-C<sub>3</sub>N<sub>4</sub>–CNT<sup>23</sup>), Ni-sulfides with Se substitution ( $\text{NiS}_{0.5}\text{Se}_{0.5}$ ,<sup>24,25</sup>), and Ni–Mn-doped Co-oxides ( $\text{CoMn}_2\text{O}_4$ ,  $\text{NiCo}_2\text{O}_4$ ,<sup>26,27</sup> which typically show good ORR and OER activity).<sup>26,27</sup> Among Co-based spinel bimetallic oxides, zinc cobaltite (ZCO)<sup>28</sup> is highly active, as  $\text{Zn}^{2+}$  and  $\text{Co}^{3+}$  occupy the tetrahedral and octahedral sites,

**Received:** July 22, 2022

**Accepted:** October 25, 2022

**Published:** November 8, 2022



respectively. This facilitates better utilization of the redox-active  $\text{Co}^{3+}$ , thus making ZCO a promising candidate.

In the past, various synthesis and engineering techniques have been adopted to improve the electrocatalytic efficiency of electrocatalysts, including tuning of morphology, various components to form a composite, introducing defects, and band engineering. Basu and co-workers grafted flower-like ZCO onto a reduced graphene oxide (RGO) sheet as an example of morphology tuning, where the authors reported enhanced electrocatalytic activity toward ORR and OER as compared to RGO and bare-ZCO.<sup>29</sup> Wang and co-workers provide a detailed perspective on designing controlled defects in a given catalyst for enhanced performance toward ORR and OER.<sup>30</sup> Furthermore, Wang et al. demonstrated improved electrocatalytic activity of carbon-supported  $\text{Co}_3\text{O}_4$  toward ORR by fine-tuning the electronic band gap.<sup>31</sup> Zhao et al. explained various methods of creating oxygen vacancies in perovskite oxides and discussed their role in improving the electrocatalytic performance of ORR.<sup>32</sup> Wang and co-workers<sup>33</sup> synthesized porous ZCO microspheres and demonstrated enhanced ORR performance to bulk ZCO. Similarly, Zhang et al. reported synthesizing porous ZCO spindle-like structures via the solvothermal method and showed improved OER performance.<sup>34</sup> In our work, we incorporated the defects in the nanoporous ZCO structure and studied their bifunctional electrocatalytic performance for ORR and OER.

In this work, we combine the hydrothermal synthesis approach with an appropriate heat treatment protocol to enhance the electrocatalytic properties of ZCO. Generally, metal oxides synthesized at ambient temperatures possess non-stoichiometry at metal and oxygen sites,<sup>35,36</sup> which is also the case in ZCO. However, the authors intentionally induced higher defects by annealing the room-temperature (RT) hydrothermally synthesized samples under vacuum to improve their electrocatalytic properties. Two sets of samples, one annealed in air—ZCO-Air and the other annealed under vacuum—ZCO-Vac, are characterized using various analytical techniques. Their electrochemical performance is quantified toward OER and ORR. The authors have also performed density functional theory (DFT)<sup>37,38</sup>-based calculations to highlight the changes in the electronic density of states (DOS) induced by defects within the ZCO structure. Significantly, the electrochemical performance of both defective samples exceeds the electrochemical activity of Pt (for ORR) and  $\text{IrO}_2$  (for OER), signifying the importance of defect-engineered ZCO in diverse energy harvesting and storage applications.

## 2. EXPERIMENTAL SECTION

**2.1. Materials.** Commercially purchased high-purity chemicals of zinc nitrate hexahydrate [ $\text{Zn}(\text{NO}_3)_2 \cdot 6\text{H}_2\text{O}$ ], cobalt nitrate hexahydrate [ $\text{Co}(\text{NO}_3)_2 \cdot 6\text{H}_2\text{O}$ ], ammonium fluoride ( $\text{NH}_4\text{F}$ ), hexamethylenetetramine (HMT), de-ionized water (DIW-resistivity of  $-18.2\text{ M}\Omega\text{ cm}$ ), and ethanol were used as received.

**2.2. Synthesis.** 2 mM cobalt nitrate, 1 mM zinc nitrate, 5 mM  $\text{NH}_4\text{F}$ , and 6 mM HMT were added to deionized water, stirred, and dissolved; the final volume was up to 300 mL. Later, the whole reaction mixture was transferred to a Teflon-lined stainless-steel vessel and kept at 180 °C in an electric furnace for 4 h. Subsequently, the reaction mixture was cooled down naturally, and the product was separated by centrifuging at 7000 rpm for 10 min and dried at 80 °C for 12 h. Finally, the samples were annealed at 400 °C for 4 h with a heating rate of 10 °C/min in two different atmospheres to get the final products: one in the ambient atmosphere in a box-type electric

furnace and the other under vacuum (4 mTorr) in a tubular furnace. These samples were named ZCO-Air and ZCO-Vac, respectively.

**2.3. Characterization.** The instrumentation used to study the electrocatalysts is presented in the *Supporting Information*.

**2.4. Electrocatalytic Activity.** The catalyst ink was prepared using the following procedure to cast on a rotating ring disk electrode (RRDE). In a typical process, 2 mg of active catalyst dispersed in the mixture of ethanol (475  $\mu\text{L}$ ) and Nafion (5 wt %—25  $\mu\text{L}$ ) solution of 500  $\mu\text{L}$ , ultrasonicated for 30 min before casting. Then, 10  $\mu\text{L}$  of dispersed catalyst ink was drop-casted on the RRDE (3 mm diameter Pt disk) and dried in the ambient atmosphere. In a conventional three-electrode configuration, catalyst-loaded RRDE, graphite rod, and Ag/AgCl were used as working the counter and reference electrodes in 0.1 M KOH electrolyte solution to study the bifunctional oxygen catalytic properties. The electrolyte solution was saturated with  $\text{N}_2$  by continuously purging  $\text{N}_2$  gas for 30 min before electrochemical studies. In this condition, cyclic voltammetry (CV), linear sweep voltammetry (LSV), and impedance measurements were carried out at different rpm to study the kinetics of the OER and ORR.

Similarly, all measurements were repeated in the  $\text{O}_2$ -saturated solution (30 min  $\text{O}_2$  purging). These two data were used to get background-corrected data for ORR. In a typical procedure, the current values of the polarization curves in  $\text{N}_2$ -saturated were subtracted from  $\text{O}_2$ -saturated ones at identical experimental parameters such as scan rate, direction, and rotation rate. All the measured data were  $iR$ -corrected using the series resistance value obtained from the impedance spectra as follows:  $E = E_{\text{RHE}} - iR$ , where  $E = iR$ -corrected potential (V),  $E_{\text{RHE}}$  = the measured potential in reversible hydrogen electrode (RHE) (V),  $i$  = the measured current before background correction (mA), and  $R$  = the series resistance determined from the impedance spectra ( $\Omega$ ).

**2.5. DFT Calculations.** All DFT calculations were performed using the Vienna Ab initio Simulation Package,<sup>39,40</sup> employing the all-electron, frozen core projector augmented wave (PAW)<sup>41</sup> theory and spin polarization without preserving any underlying structural symmetry. The authors used the Hubbard  $U$ -corrected<sup>42,43</sup> strongly constrained and appropriately normed (i.e., SCAN +  $U$ )<sup>44–46</sup> functional to model the electronic exchange and correlation, where the PAW potentials used are identical to our previous work.<sup>46</sup> We used a plane-wave basis with a kinetic energy cutoff of 520 eV to describe the electronic one-electron wavefunctions. For the relaxation of all structures, we used convergence criteria of 0.01 meV and  $<0.031\text{ eV}/\text{\AA}$  on the total energies and atomic forces, respectively. For relaxing the structure of bulk ZCO, we sampled the irreducible Brillouin zone using a  $\Gamma$ -centered  $k$ -point grid with a density of 32  $k$ -points per  $\text{\AA}$  (KPPA). In contrast, for both ZCO-Air and ZCO-Vac structures (which contain Zn and O deficiency), we utilized a  $\Gamma$ -centered grid with a density of 24 KPPA to reduce computational costs. Upon structure relaxation of ZCO-Air and ZCO-Vac, we performed a single self-consistent field calculation with a  $\Gamma$ -centered grid of density 32 KPPA to ensure that the computed energies can be compared with the bulk structure. Note that the cell volume, shape, and ionic positions can change for bulk ZCO, while only ionic positions can change for ZCO-Air and ZCO-Vac during relaxation. For bulk ZCO, we used the conventional unit cell as obtained from the Inorganic Crystal Structure Database,<sup>47</sup> while for ZCO-Air and ZCO-Vac, the authors used a  $2 \times 2 \times 1$  and a  $2 \times 1 \times 1$  supercell, respectively, of the relaxed conventional cell of bulk ZCO. Details on the choice of supercell sizes for the defective structures and the steps taken for enumerating defective configurations, done using the pymatgen<sup>48</sup> library, are detailed in the *Supporting Information*. For calculating the DOS of the relaxed bulk ZCO structure, we used a  $\Gamma$ -centered  $k$ -point grid with a density of 96 KPPA (with the new  $k$ -points added at zero weight to the set of  $k$ -points used for structure relaxation) and sampled the electronic energies from  $-20$  to  $20\text{ eV}$  in steps of 0.005 eV. Similarly, for the DOS calculations of ZCO-Air and ZCO-Vac structures, we used a  $\Gamma$ -centered grid of density 32 and 64 KPPA, respectively. All our DOS calculations involved doing a single “fake” self-consistent calculation at the SCAN +  $U$  level of theory.

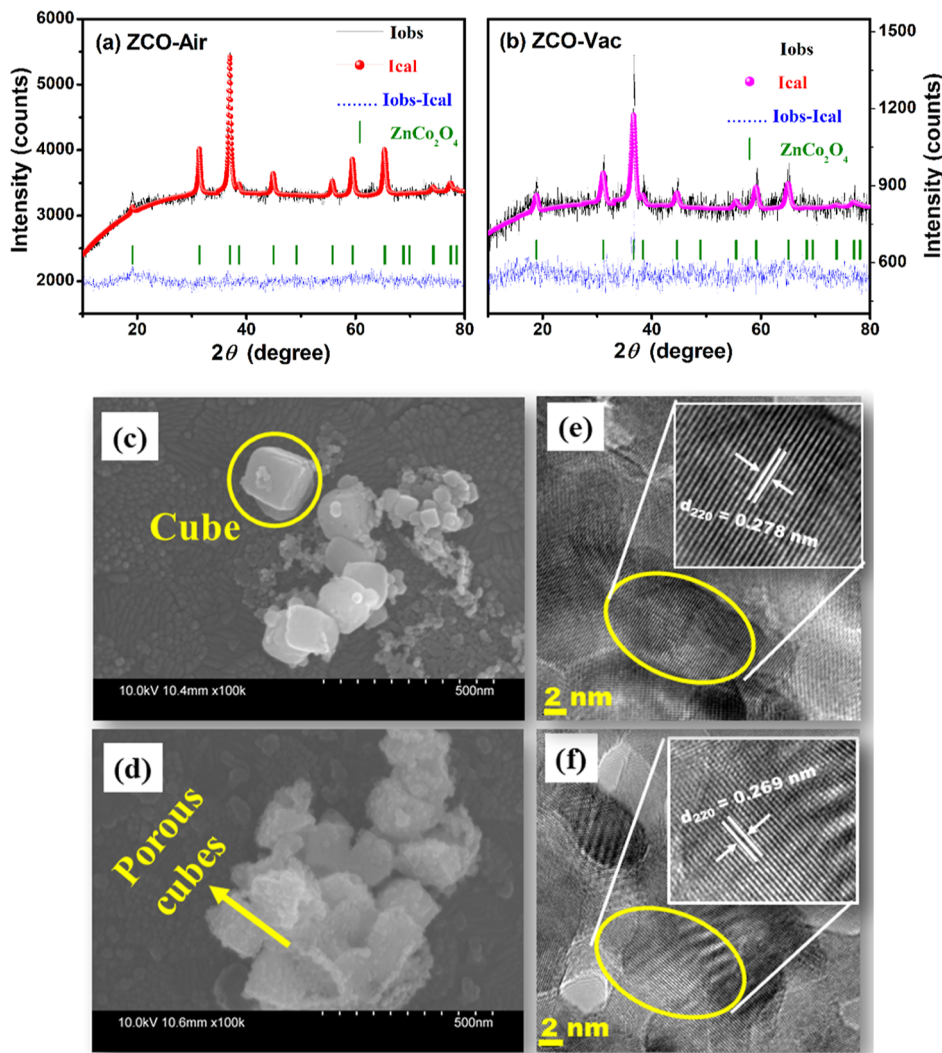


**Figure 1.** Rietveld-refined XRD data of (a) ZCO-Air and (b) ZCO-Vac samples. Black and red/magenta traces correspond to observed and calculated intensities, with blue dots representing the difference profile. Green dashes represent peaks observed in a standard ZCO crystal. SEM and TEM images of (c,e) ZCO-Air and (d,f) ZCO-Vac samples show cubic morphology and their respective insets show the \$d\$-spacing values of the samples.

**Table 1.** Rietveld Refinement Parameters of ZCO Samples

sample	formula sum	space group	lattice parameters		position parameters					goodness of fit
			a = b = c (\$\text{\AA}\$)	V (\$\text{\AA}^3\$)	atom	occupancy	x	y	z	
ZCO-Air	Zn <sub>7.78</sub> Co <sub>16.00</sub> O <sub>31.29</sub>	\$Fd\bar{3}m\$ (227)	8.098 (2)	531.14	Zn	0.96	0.375	0.375	0.375	0.99
ZCO-Vac	Zn <sub>6.52</sub> Co <sub>16.00</sub> O <sub>28.66</sub>	\$Fd\bar{3}m\$ (227)	8.112 (6)	533.78	Zn	0.81	0.375	0.375	0.375	0.96
					Co	1	0	0	0	
					O	0.98	0.245	0.245	0.245	
					Zn	0.81	0.375	0.375	0.375	
					Co	1	0	0	0	
					O	0.89	0.238	0.238	0.238	

### 3. RESULTS AND DISCUSSION

**3.1. Structure and Morphology.** Figure 1a,b shows the refined X-ray diffraction (XRD) structures of ZCO-Air and ZCO-Vac. Both the samples show similar XRD patterns as a standard ZnCo<sub>2</sub>O<sub>4</sub> crystal structure with space group \$Fd\bar{3}m\$.<sup>49</sup> However, the samples have different peak intensities, full-width-at-half-maxima (FWHM), and peak positions. The broadening of the dominant XRD peak of ZCO-Vac compared to ZCO-Air suggests a smaller crystallite size for the vacuum annealed sample. The unit cell parameters of ZCO-Air ( $a = b = c = 8.098 \text{ \AA}$ , and  $V = 531.14 \text{ \AA}^3$ ) are lower as compared to those of ZCO-Vac ( $a = b = c = 8.112 \text{ \AA}$ , and  $V = 533.78 \text{ \AA}^3$ ). The occupancy parameters (OPs) are refined for both samples and listed in Table 1. No OP variations are observed in the Co elements in both the samples, whereas the OP changed from 0.96 to 0.81 for Zn and from 0.98 to 0.89 for O of the samples, respectively. Binary or ternary metal oxides have been reported to show metal/oxygen vacancy/deficiency in the synthesized samples in the ambient atmosphere.<sup>50,51</sup> ZCO-Air and ZCO-Vac samples exhibit Zn and O vacancy/deficiency, with the

$c = 8.098 \text{ \AA}$ , and  $V = 531.14 \text{ \AA}^3$ ) are lower as compared to those of ZCO-Vac ( $a = b = c = 8.112 \text{ \AA}$ , and  $V = 533.78 \text{ \AA}^3$ ). The occupancy parameters (OPs) are refined for both samples and listed in Table 1. No OP variations are observed in the Co elements in both the samples, whereas the OP changed from 0.96 to 0.81 for Zn and from 0.98 to 0.89 for O of the samples, respectively. Binary or ternary metal oxides have been reported to show metal/oxygen vacancy/deficiency in the synthesized samples in the ambient atmosphere.<sup>50,51</sup> ZCO-Air and ZCO-Vac samples exhibit Zn and O vacancy/deficiency, with the

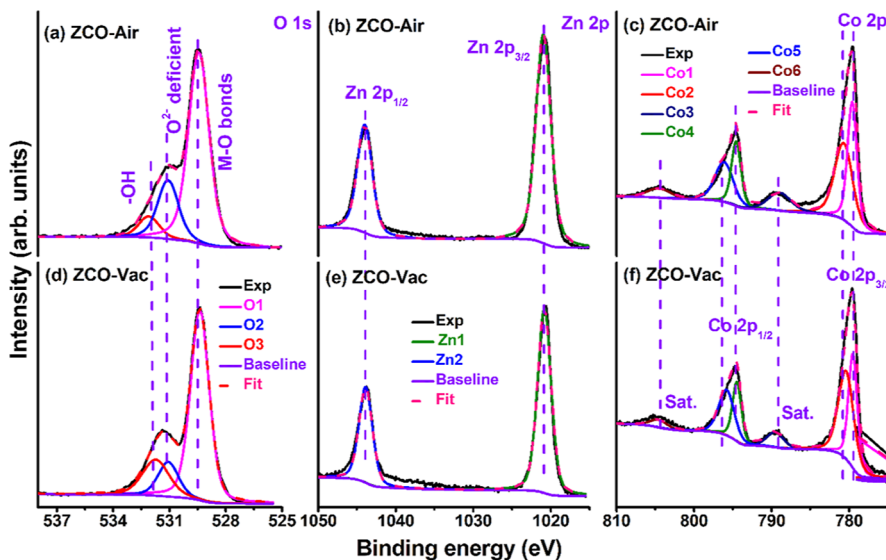


**Figure 2.** Core-level XPS of O 1s (a,d), Zn 2p (b,e), and Co 2p (c,f) of ZCO-Air and ZCO-Vac.

vacancy/deficiency being higher in ZCO-Vac (cf. Table 1). Therefore, annealing in vacuum conditions induces a higher defect concentration in ZCO than the as-synthesized or air-annealed sample.

Scanning electron microscopy (SEM) images of ZCO-Air and ZCO-Vac are given in Figure 1c,d. Although the morphology of both the samples appears similar (cubic), differences in porosity can be seen in the higher magnification micrographs (Figure S1). The ZCO-Air sample has highly rigid surfaces (cf. Figure 1c), whereas the ZCO-Vac sample shows porous cubic shapes (cf. Figure 1d). Both the samples are formed by the self-assembly of nanoparticles, which generally occurs via Ostwald ripening.<sup>51</sup> Transmission electron microscopy (TEM) and high-resolution TEM images (Figure S2a,b) of ZCO-Air and ZCO-Vac (Figure S2d,e) samples also indicate higher porosity for the vacuum-annealed sample compared to the air-annealed sample and do signify self-assembly of nanoparticles. The estimated *d*-spacing values are slightly higher for ZCO-Air (0.278 nm, inset of Figure 1e) than for ZCO-Vac (0.269 nm, inset of Figure 1f). Selective area electron diffraction (SAED, Figure S2c,f) patterns of both samples reveal that ZCO-Air has higher crystallinity than ZCO-Vac, which is in line with the XRD results.

**3.2. Surface Properties.** Figure 2 compares the surface states of the samples, as characterized via X-ray photoemission spectroscopy (XPS). The XPS broad spectra of both samples (Figure S3) show peaks corresponding to O, Zn, Co, and C elements (C, observed due to the sample preparation for XPS measurements under non-vacuum conditions). O 1s spectra of ZCO-Air (Figure 2a) display three peaks corresponding to Zn/Co–O bonds (O1: 529.5 eV), O<sup>2-</sup> deficiency (O2: 531.1 eV), and –OH groups (O3: 532.1 eV), while the ZCO-Vac (Figure 2d) has similar peaks near O1: 529.4 eV, O2: 531.0 eV, and O3: 531.9 eV, respectively. Zn 2p spectra (Figure 2b,e) of both the samples show doublets of the spin-orbit split of Zn 2p<sub>1/2</sub> and Zn 2p<sub>3/2</sub> at 1044.0/1043.9 and 1021.0/1020.9 eV for ZCO-Air and ZCO-Vac, respectively. The energy difference between these Zn 2p<sub>1/2</sub>/2p<sub>3/2</sub> peaks is ~23 eV, which corroborates previous lattice reports of standard Zn<sup>2+</sup> states.<sup>52</sup> Co 2p spectra (Figure 2c,f) of both the samples display three sets of doublet peaks: the spin-orbit split of Co 2p<sub>1/2</sub> and Co

2p<sub>3/2</sub> for (i) Co<sup>2+</sup> and (ii) Co<sup>3+</sup> states, and (iii) satellite peaks. Co 2p<sub>3/2</sub> states for Co<sup>3+</sup>/Co<sup>2+</sup> are at 779.6/780.7 and 779.5/780.4 eV in ZCO-Air and ZCO-Vac, respectively, while for Co 2p<sub>1/2</sub>, the corresponding peaks were observed at 794.6/796.1 eV (ZCO-Air) and 794.5/795.8 eV (ZCO-Vac). Therefore, XPS data indicate that Co exists in both +2 and +3 states in both samples.<sup>53–56</sup> The at % of O, Zn, and Co are 57.85, 22.29, and 19.86 for ZCO-Air and 63.92, 17.35, and 18.73 for ZCO-Vac, respectively (Table 2). The deficiency of O and Zn for ZCO-Vac is higher than that for the ZCO-Air samples, which supports our XRD refinement.

Annealing-atmosphere-dependent porosity variation of the samples is analyzed and compared by N<sub>2</sub> adsorption and desorption profiles, as presented in Figure S4. The surface area, pore volume, and pore size are 37.57 m<sup>2</sup> g<sup>-1</sup>, 0.132 cm<sup>3</sup> g<sup>-1</sup>, and 11.61 nm for ZCO-Air and 44.32 m<sup>2</sup> g<sup>-1</sup>, 0.082 cm<sup>3</sup> g<sup>-1</sup>, and 6.76 nm for ZCO-Vac, respectively (cf. Table in the inset of Figure S4). The surface area of ZCO-Vac is ~20% higher than that of the ZCO-Air sample because of a higher surface porosity observed in the SEM images (cf. Figure 1d). Due to this higher surface area, the ZCO-Vac catalyst will provide a larger effective contact area for redox reactions.

**3.3. Electrochemical Studies.** First, the catalytic activity of the ZCO samples and the standard Pt/C is examined by measuring CV in 0.1 M KOH electrolyte solution saturated with N<sub>2</sub> and O<sub>2</sub>. Figure 3 shows the CV curves of all samples measured against a RHE. While no redox events are observed in the N<sub>2</sub>-saturated electrolyte (dashed black lines in Figure S5 for ZCO-Vac), clear peaks are observed in the O<sub>2</sub>-saturated electrolyte (dashed red lines in Figure S5 for ZCO-Vac). This indicates that the ZCO samples are electrochemically active toward ORR. Furthermore, the peak current of the ZCO-Vac sample (blue lines in Figure 3) is significantly higher in magnitude than standard Pt/C (black line). This result signifies that the ZCO-Vac sample, with its porous morphology and larger surface area, provides more ORR catalytic sites. The electrochemical active surface area (ECSA) for both ZCO samples is determined by measuring CV at different scan rates (Figures S6 and S7). The ECSA values for ZCO-Air and ZCO-Vac are 6.02 and 7.92 cm<sup>-2</sup>, respectively (Figure S8). With

sample	peak binding energy (eV $\pm$ 0.2)/(relative atomic concentration (%))/[fwhm (eV)]											
	O1	O2	O3	Zn1	Zn2	Co1	Co3	Co2	Co4	O	Zn	Co
ZCO-Air	529.5 (40.77) [1.30]	531.1 (12.56) [1.30]	532.1 (4.52) [1.30]	1021.0 (22.29) [2.30]	1044.0 (9.13) [1.46]	779.6 (9.13) [1.46]	794.6	780.7 (10.73) [2.78]	796.1	57.85	22.29	19.86
ZCO-Vac	529.4 (37.58) [1.18]	531.0 (14.61) [1.18]	531.9 (11.73) [1.18]	1020.9 (17.35) [2.06]	1043.9	779.5 (8.09) [1.36]	794.5	780.4 (10.64) [2.35]	795.8	63.92	17.35	18.73

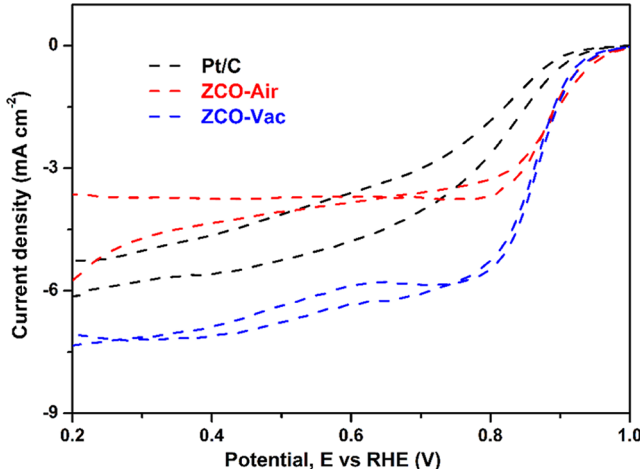


**Figure 3.** CV of ZCO samples and standard Pt/C in O<sub>2</sub>-saturated 0.1 M KOH at 1600 rpm with a scan rate of 10 mV s<sup>-1</sup>. The ZCO-Vac sample shows higher peak current density values than Pt/C.

larger ECSA, ZCO-Vac is expected to show higher electrocatalytic activity toward ORR and OER.

LSVs for standard Pt/C and ZCO samples in O<sub>2</sub> saturated 0.1 M KOH solution are shown in Figure 4a. The ORR half-wave potential values of ZCO-Vac and ZCO-Air samples are approximately 0.88 and 0.85 V, respectively, which is better than the standard Pt/C (0.80 V). All LSVs in the paper are *iR*- and background-corrected (Figure S9). For comparison, the ORR data of samples were also recorded using Pt as a counter electrode in the three-electrode setup, and the corresponding figures and discussion are added in the Supporting Information (Figure S10). Tafel plots of ZCO samples are given in the inset of Figure 4a, which exhibit slopes of 68.2, 63.7, and 62.4 mV dec<sup>-1</sup> for Pt/C, ZCO-Air, and ZCO-Vac, respectively. Thus, ZCO samples have a lower Tafel slope than the standard Pt/C. Notably, ZCO-Vac, with its porous morphology and larger ECSA value, provides more catalytic sites and thereby shows higher electrocatalytic activity toward ORR than ZCO-Air and Pt/C. The broad current plateau in both ZCO samples highlights the four-electron pathway for ORR.<sup>29</sup> The parallel straight lines with nearly equal slopes in the Koutecky–Levich (K–L) plots (Figure 4b,c) indicate first-order kinetics, rate-determined by the four-electron pathway mechanism for ORR. Moreover, the electron-transfer number calculated from the K–L plots is ~3.70–3.75 for ZCO-Air (Figure 4b) and 3.93–4.0 for ZCO-Vac (Figure 4c), which suggests a higher catalytic activity for the ZCO-Vac toward the four-electron oxygen reduction process.

Furthermore, we carried out rotating ring disc electrode (RRDE) measurements at various rotation speeds for both ZCO samples in O<sub>2</sub>-saturated 0.1 M KOH solution. The LSV curves measured at disk and ring currents are depicted in Figure S11 for ZCO-Air and Figure S12 for ZCO-Vac. The electron-transfer number is nearly equal to 4 for both ZCO samples using the RRDE measurements, as shown in Figure S13, which is similar to the electron-transfer number calculated from K–L plots. The formation of H<sub>2</sub>O<sub>2</sub> (peroxide)% is also shown in Figure S13.

We further studied the OER activity of these samples by performing LSV in N<sub>2</sub>-saturated 0.1 M KOH solution at 1600 rpm. ZCO-Vac and ZCO-Air show overpotentials of 0.51 and 0.53 V for OER, respectively, to achieve the current density of

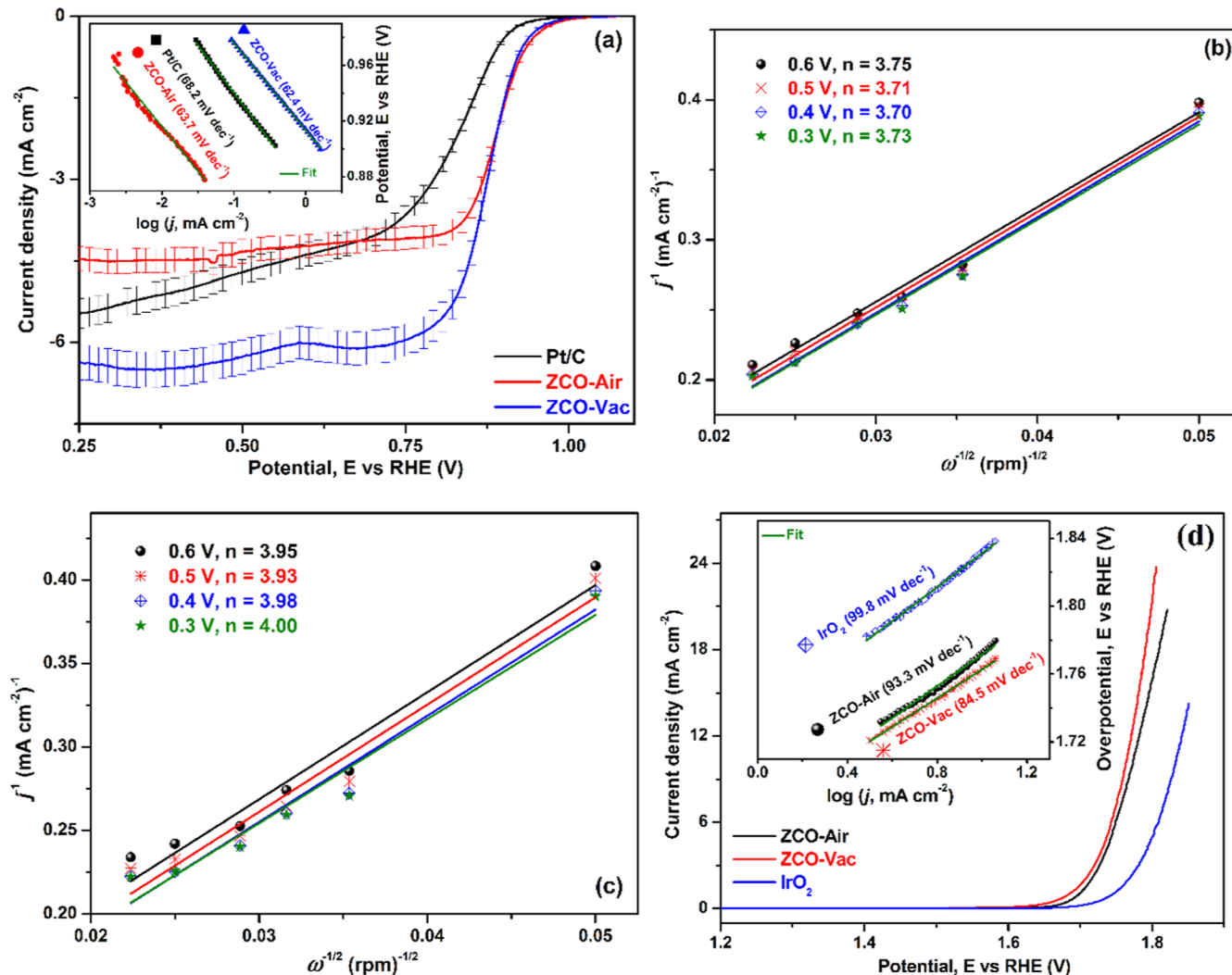


**Figure 4.** (a) LSV curves ( $iR$ - and background-corrected) and Tafel plots (inset of the figure) of the catalytic ORR process of ZCO-Air, ZCO-Vac, and Pt/C at a rotation rate of 1600 rpm with a scan rate of  $10 \text{ mV s}^{-1}$ . K-L plots at various potentials (vs RHE) for ZCO-Air (b) and ZCO-Vac (c). Comparison of LSV curves ( $iR$ -corrected) and Tafel plots (inset of the figure) of the catalytic OER process of the ZCO samples in  $\text{N}_2$ -saturated  $0.1 \text{ M KOH}$  at a rotation rate of 1600 rpm with a scan rate of  $10 \text{ mV s}^{-1}$  (d).

**Table 3. Comparison of the Oxygen Catalytic Activity of Reported ZCO Composite, Bare ZCO, and Our Samples**

catalyst with composition	ORR (V versus RHE) at $I = -3 \text{ mA/cm}^2$	OER (V versus RHE) at $I = 10 \text{ mA/cm}^2$	$\Delta E = E_{\text{OER}} - E_{\text{ORR}}$	activity/reference
ZnCo <sub>2</sub> O <sub>4</sub>	0.696		1.64	ORR/OER <sup>29</sup>
RGO-ZnCo <sub>2</sub> O <sub>4</sub>	0.851		1.53	ORR/OER <sup>29</sup>
ZnCo <sub>2</sub> O <sub>4</sub> /N-CNT	0.75		1.65	ORR/OER <sup>58</sup>
ZnCo <sub>2</sub> O <sub>4</sub> /Co <sub>3</sub> O <sub>4</sub> /NC-CNT		1.61		OER <sup>54</sup>
ZnCo <sub>2</sub> O <sub>4</sub>	0.70			ORR <sup>59</sup>
lilac flower-shaped-ZnCo <sub>2</sub> O <sub>4</sub>	0.75 (at $I = -2 \text{ mA/cm}^2$ )			ORR <sup>60</sup>
ZnCo <sub>2</sub> O <sub>4</sub> -nanosheets	0.62	1.57	0.95	ORR/OER <sup>61</sup>
mesoporous ZnCo <sub>2</sub> O <sub>4</sub>	0.72	1.60	0.88	ORR/OER <sup>62</sup>
ZCO-Vac	0.88	1.75	0.87	Present work
ZCO-Air	0.85	1.77	0.92	Present work

$10 \text{ mA/cm}^2$  (Figure 4d). These overpotentials are slightly higher than that of ZCO composites.<sup>29</sup> The Tafel plots for OER are given in the inset of Figure 4d, where ZCO-Air shows a Tafel slope of  $93.3 \text{ mV dec}^{-1}$  and ZCO-Vac displays a slightly lower slope of  $84.5 \text{ mV dec}^{-1}$ . Tafel slopes of both ZCO samples are better than those of the standard IrO<sub>2</sub> ( $99.8 \text{ mV dec}^{-1}$ ), further supporting the use of defective-ZCO (ZCO-Vac) as a bifunctional oxygen electrocatalyst.

The impedance spectra of both ZCO samples and standard Pt/C and IrO<sub>2</sub> show similar features in high- and low-frequency regions (Figure S14), highlighting that both the samples and standard Pt/C and IrO<sub>2</sub> have nearly identical resistance values ( $37\text{--}40 \Omega$ ) and similar kinetics for ORR and OER processes. The ORR catalytic activity of the ZCO-Vac sample is comparable to reported ZCO composites and shows better activity than that of defect-free ZCO (cf. Table 3).<sup>29</sup>

We analyze the stability of the ZCO samples by performing chronoamperometry (CA) measurements in O<sub>2</sub> (ORR) and N<sub>2</sub> (OER)-saturated 0.1 M KOH solution, as displayed in Figure S15 and its inset, respectively. As observed in the ORR stability plot (Figure S15), the current density remains at ~95% for ZCO-Vac compared to ZCO-Air (78%) even after 6 h, highlighting the stability of the ZCO-Vac sample. Similarly, higher current density retention of 93% for ZCO-Vac than ZCO-Air (75%) was obtained in the OER after 6 h of CA (inset of Figure S15). Moreover, both catalysts retained their initial morphology (Figure S16) even after the CA test, suggesting higher stability of the catalysts. Figure 5 combines

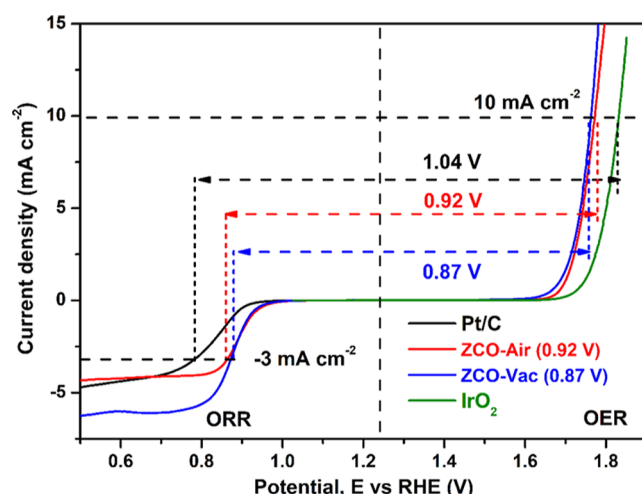


**Figure 5.** Combined LSV curves (bifunctional activity) of ZCO samples with standard Pt/C and IrO<sub>2</sub> were measured in O<sub>2</sub>/N<sub>2</sub>-saturated 0.1 M KOH at a rotation rate of 1600 rpm with a scan rate of 10 mV s<sup>-1</sup>.

the LSVs of both OER and ORR to investigate the potential range where the oxygen catalytic reactions occur. The ZCO-Vac sample shows OER and ORR catalytic activity with a potential difference of 0.87 V. In contrast, the ZCO-Air sample displays a corresponding potential difference of 0.92 V (marginally higher than ZCO-Vac). The porous nature and the surface defects contribute to the larger ECSA of ZCO-Vac, which resulted in enhanced ORR and OER electrocatalytic performance than ZCO-Air.

The formation of oxygen vacancies at the surface requires smaller energy when compared to the energy required to form vacancies in the bulk of ZCO. Thus, ZCO-Vac has a higher number of vacancies, which acts as adsorption sites for ORR and OER. The presence of oxygen vacancies on the surface of ZCO-Vac influences oxygen adsorption during the ORR and OER by changing the surface chemistry, such as active site, elemental composition, and -OH at the surface. Thus, ZCO-Vac with higher surface oxygen vacancies shows better bifunctional oxygen catalytic activity than ZCO-Air.

**3.4. DFT Calculations.** To explore the fundamental structural reasons contributing to the better observed electrocatalytic performance of defective ZCO versus the standard Pt/C/IrO<sub>2</sub> samples and especially defect-free ZCO,<sup>29</sup> we calculated the electronic DOS, which is displayed in Figure 6. Our calculations predict a semiconducting behavior for both bulk and defective ZCO (i.e., ZCO-Air and ZCO-Vac structures), as indicated by the band gap values on each panel of Figure 6. The predicted band gap of bulk ZCO (1.82 eV) is lower than the reported optical band gaps (2.4–3.2 eV),<sup>57</sup> which is expected of a ground state theoretical framework such as SCAN + U.<sup>46</sup> The nature of the valence and conduction band edges (VBE and CBE) also change qualitatively from bulk ZCO (where O p states do play a role at the VBE) to ZCO-Air and ZCO-Vac (where only Co d states are at the VBE), highlighting the redox-activity of Co and the co-existence of Co<sup>2+/3+</sup> ions upon Zn and O vacancy formation, in agreement with our XPS measurements (Figure 2).

Significantly, we predict that the band gaps decrease monotonically from bulk ZCO (1.82 eV, Figure 6a) to ZCO-Air (0.73 eV, Figure 6b), and eventually ZCO-Vac (0.64 eV, Figure 6c), and indicating that a qualitatively similar trend may be observed in experiments as well. Note that a robust bifunctional electrocatalyst must exhibit an “optimal” bulk band gap so that it is equally efficient at both ORR (a reduction reaction) and OER (an oxidation reaction). Hence, we expect that defects in ZCO (during synthesis and especially during heat treatment) play a critical role in reducing the bulk band gap to more optimal levels, which enhances the electrocatalytic performance of defective ZCO, especially against defect-free ZCO.<sup>29</sup> Thus, in addition to the band gap reduction by the defects, the formation of a porous morphology further promotes catalytic reactions, resulting in

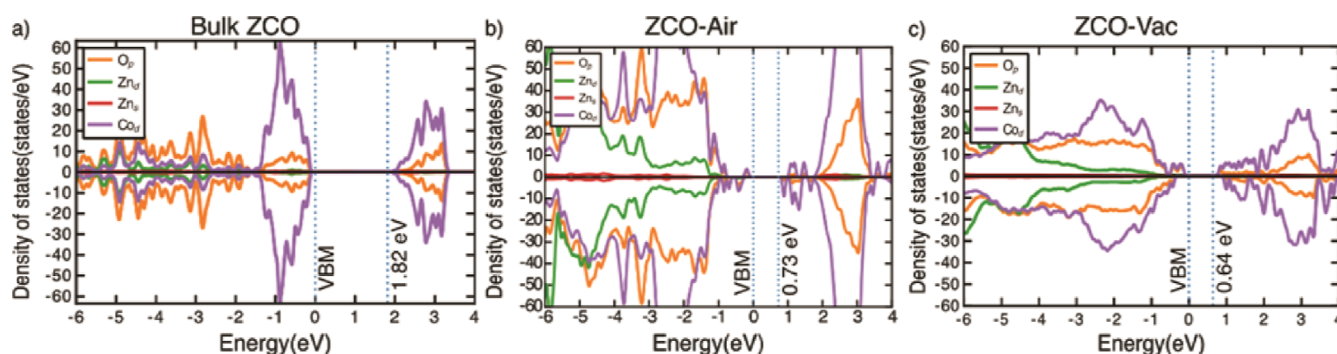


**Figure 6.** Electronic DOS of bulk (a), air-annealed (b), and vacuum-annealed (c) structures of ZCO, as calculated using SCAN + U. Orange, green, red, and purple lines indicate O p, Zn d, Zn s, and Co d states. Positive (negative) DOS values correspond to up (down) spin electrons. The band edges are indicated by dotted blue lines with the zero on the energy scale arbitrarily set to the valence band maximum. The text annotation indicates the band gap of each structure within each panel.

defective-ZCO outperforming the standard Pt/C and IrO<sub>2</sub> for ORR and OER, respectively.

## 4. CONCLUSIONS

We synthesized ZCO-Vac and ZCO-Air samples via a hydrothermal method and demonstrated their electrocatalytic activity toward ORR and OER. The refined data from XRD suggested the existence of Zn and O vacancies in both samples, with ZCO-Vac exhibiting a higher concentration of Zn and O vacancies than ZCO-Air. ZCO-Vac displayed porous nanocubes with a larger ECSA than the ZCO-Air sample. Subsequently, we found that ZCO-Air and ZCO-Vac show better ORR activity than the standard Pt/C sample and a better OER activity (overpotential) than the standard IrO<sub>2</sub>. In the case of ORR, we expect the reaction to occur via a 4e<sup>-</sup> pathway forming H<sub>2</sub>O from O<sub>2</sub> without forming other intermediates such as H<sub>2</sub>O<sub>2</sub>. ZCO-Vac shows higher oxygen bifunctional activity and is more stable than ZCO-Air because of its porous nature, higher defects, larger ECSA, and possibly a more “optimal” band gap than ZCO-Air (or bulk ZCO), as indicated by the DOS calculations. Thus, current work demonstrates a high degree of electrocatalytic activity of ZCO-Vac toward oxygen reduction and evolution reactions, making an appropriately synthesized and heat-treated ZCO a likely bifunctional catalyst for metal–air batteries, fuel cells, and other applications.

## ■ ASSOCIATED CONTENT

### Supporting Information

The Supporting Information is available free of charge at <https://pubs.acs.org/doi/10.1021/acsaem.2c02257>.

Physicochemical characterization, electrochemical measurements, SEM images, TEM images, XPS survey scan, BET curves, CV curves of ZCO-Vac, ECSA analysis, background- and *iR*-corrected LSV curves, comparison of LSV curves at different counter electrodes, electron transfer plots, impedance spectra, CA of both samples for ORR/OER, SEM after CA, structural models, and workflow for DFT calculations ([PDF](#))

## ■ AUTHOR INFORMATION

### Corresponding Authors

**Gopalakrishnan Sai Gautam** – Department of Materials Engineering, Indian Institute of Science, Bengaluru 560012, India;  [orcid.org/0000-0002-1303-0976](https://orcid.org/0000-0002-1303-0976); Email: [saigautamg@iisc.ac.in](mailto:saigautamg@iisc.ac.in)

**Aninda J. Bhattacharyya** – Solid State and Structural Chemistry Unit, Indian Institute of Science, Bengaluru 560012, India;  [orcid.org/0000-0002-0736-0004](https://orcid.org/0000-0002-0736-0004); Email: [anindajb@iisc.ac.in](mailto:anindajb@iisc.ac.in)

### Authors

**Gowra Raghupathy Dillip** – Energy Institute, Centre of Rajiv Gandhi Institute of Petroleum Technology, Bengaluru 560064, India;  [orcid.org/0000-0001-6855-2192](https://orcid.org/0000-0001-6855-2192)

**Gundegowda Kalligowdanadoddi Kiran** – Solid State and Structural Chemistry Unit, Indian Institute of Science, Bengaluru 560012, India;  [orcid.org/0000-0002-1355-8826](https://orcid.org/0000-0002-1355-8826)

**Abhishek Bharti** – Solid State and Structural Chemistry Unit, Indian Institute of Science, Bengaluru 560012, India

**Tanmay Mohan Bhagwat** – Department of Materials Engineering, Indian Institute of Science, Bengaluru 560012, India

Complete contact information is available at: <https://pubs.acs.org/10.1021/acsaem.2c02257>

### Author Contributions

<sup>†</sup>G.R.D. and G.K.K. contributed equally.

### Notes

The authors declare no competing financial interest.

## ■ ACKNOWLEDGMENTS

G.R.D. acknowledges the Department of Science and Technology, New Delhi, India, for the award of the DST-INSPIRE Faculty (DST/INSPIRE//04/2018/000358). G.K.K. acknowledges the financial support of the University Grants Commission, Govt. of India, through the D.S. Kothari post-doctoral Fellowship. A.J.B. thanks DST, the Government of India, for support under MECSP (DST/TMD/MECSP/2K17/07). We acknowledge the computational resources provided by the Supercomputer Education and Research Centre, Indian Institute of Science, for enabling some of the DFT calculations showcased in this work.

## ■ REFERENCES

- (1) Steele, B. C. H.; Heinzel, A. Materials for Fuel-Cell Technologies. *Nature* **2001**, *414*, 345–352.
- (2) Bruce, P. G.; Freunberger, S. A.; Hardwick, L. J.; Tarascon, J. M. Li<sub>2</sub>O<sub>2</sub> and Li<sub>2</sub>S Batteries with High Energy Storage. *Nat. Mater.* **2012**, *11*, 19–29.
- (3) Luo, J.; Im, J. H.; Mayer, M. T.; Schreier, M.; Nazeeruddin, M. K.; Park, N. G.; Tilley, S. D.; Fan, H. J.; Grätzel, M. Water Photolysis at 12.3% Efficiency via Perovskite Photovoltaics and Earth-Abundant Catalysts. *Science* **2014**, *345*, 1593–1596.
- (4) Lefèvre, M.; Proietti, E.; Jaouen, F.; Dodelet, J. P. Iron-Based Catalysts with Improved Oxygen Reduction Activity in Polymer Electrolyte Fuel Cells. *Science* **2009**, *324*, 71–4.
- (5) Suntivich, J.; Gasteiger, H. A.; Yabuuchi, N.; Nakanishi, H.; Goodenough, J. B.; Shao-Horn, Y. Design Principles for Oxygen-Reduction Activity on Perovskite Oxide Catalysts for Fuel Cells and Metal-Air Batteries. *Nat. Chem.* **2011**, *3*, 546–550.
- (6) Liao, L.; Zhang, Q.; Su, Z.; Zhao, Z.; Wang, Y.; Li, Y.; Lu, X.; Wei, D.; Feng, G.; Yu, Q.; Cai, X.; Zhao, J.; Ren, Z.; Fang, H.; Robles-Hernandez, F.; Baldelli, S.; Bao, J. Efficient Solar Water-Splitting Using a Nanocrystalline CoO Photocatalyst. *Nat. Nanotechnol.* **2014**, *9*, 69–73.
- (7) Tian, X.; Lu, X. F.; Xia, B. Y.; Lou, X. W. Advanced Electrocatalysts for the Oxygen Reduction Reaction in Energy Conversion Technologies. *Joule* **2020**, *4*, 45–68.
- (8) Marković, N. M.; Schmidt, T. J.; Stamenković, V.; Ross, P. N. Oxygen Reduction Reaction on Pt and Pt Bimetallic Surfaces: A Selective Review. *Fuel Cells* **2001**, *1*, 105–116.
- (9) Hu, Y.; Zhang, H.; Wu, P.; Zhang, H.; Zhou, B.; Cai, C. Bimetallic Pt-Au Nanocatalysts Electrochemically Deposited on Graphene and Their Electrocatalytic Characteristics towards Oxygen Reduction and Methanol Oxidation. *Phys. Chem. Chem. Phys.* **2011**, *13*, 4083–4094.
- (10) Giovanni, M.; Poh, H. L.; Ambrosi, A.; Zhao, G.; Sofer, Z.; Šaněk, F.; Khezri, B.; Webster, R. D.; Pumera, M. Noble Metal (Pd, Ru, Rh, Pt, Au, Ag) Doped Graphene Hybrids for Electrocatalysis. *Nanoscale* **2012**, *4*, 5002–5008.
- (11) Lee, Y.; Suntivich, J.; May, K. J.; Perry, E. E.; Shao-Horn, Y. Synthesis and Activities of Rutile IrO<sub>2</sub> and RuO<sub>2</sub> Nanoparticles for Oxygen Evolution in Acid and Alkaline Solutions. *J. Phys. Chem. Lett.* **2012**, *3*, 399–404.

- (12) Kong, F. D.; Zhang, S.; Yin, G. P.; Wang, Z. B.; Du, C. Y.; Chen, G. Y.; Zhang, N. Electrochemical Studies of Pt/Ir-IrO<sub>2</sub> Electrocatalyst as a Bifunctional Oxygen Electrode. *Int. J. Hydrogen Energy* **2012**, *37*, 59–67.
- (13) Huang, F. H.; Wang, J.; Peng, Y.; Jung, C. Y.; Fisher, A.; Wang, X. Design of Efficient Bifunctional Oxygen Reduction/Evolution Electrocatalyst: Recent Advances and Perspectives. *Adv. Mater.* **2017**, *7*, 1700544.
- (14) Gong, K.; Du, F.; Xia, Z.; Durstock, M.; Dai, L. Nitrogen-Doped Carbon Nanotube Arrays with High Electrocatalytic Activity for Oxygen Reduction. *Science* **2009**, *323*, 760–764.
- (15) Chai, G. L.; Hou, Z.; Shu, D. J.; Ikeda, T.; Terakura, K. Active Sites and Mechanisms for Oxygen Reduction Reaction on Nitrogen-Doped Carbon Alloy Catalysts: Stone-Wales Defect and Curvature Effect. *J. Am. Chem. Soc.* **2014**, *136*, 13629–13640.
- (16) Chai, G. L.; Qiu, K.; Qiao, M.; Titirici, M. M.; Shang, C.; Guo, Z. Active Sites Engineering Leads to Exceptional ORR and OER Bifunctionality in P,N Co-Doped Graphene Frameworks. *Energy Environ. Sci.* **2017**, *10*, 1186–1195.
- (17) Fink, M. F.; Eckhardt, J.; Khadke, P.; Gerdes, T.; Roth, C. Bifunctional  $\alpha$ -MnO<sub>2</sub> and Co<sub>3</sub>O<sub>4</sub> Catalyst for Oxygen Electrocatalysis in Alkaline Solution. *Chemelectrochem* **2020**, *7*, 4822–4836.
- (18) Guo, Y.; Tang, J.; Qian, H.; Wang, Z.; Yamauchi, Y. One-Pot Synthesis of Zeolitic Imidazolate Framework 67-Derived Hollow Co<sub>3</sub>S<sub>4</sub>@MoS<sub>2</sub> Heterostructures as Efficient Bifunctional Catalysts. *Chem. Mater.* **2017**, *29*, 5566–5573.
- (19) Tang, Y.; Jing, F.; Xu, Z.; Zhang, F.; Mai, Y.; Wu, D. Highly Crumpled Hybrids of Nitrogen/Sulfur Dual-Doped Graphene and Co<sub>9</sub>S<sub>8</sub> Nanoplates as Efficient Bifunctional Oxygen Electrocatalysts. *ACS Appl. Mater. Interfaces* **2017**, *9*, 12340–12347.
- (20) Zhang, Z.; Zhang, T.; Lee, J. Y. Electrochemical Performance of Borate-Doped Nickel Sulfide: Enhancement of the Bifunctional Activity for Total Water Splitting. *Chemelectrochem* **2019**, *6*, 1443–1449.
- (21) Feng, X.; Jiao, Q.; Cui, H.; Yin, M.; Li, Q.; Zhao, Y.; Li, H.; Zhou, W.; Feng, C. One-Pot Synthesis of NiCo<sub>2</sub>S<sub>4</sub> Hollow Spheres via Sequential Ion-Exchange as an Enhanced Oxygen Bifunctional Electrocatalyst in Alkaline Solution. *ACS Appl. Mater. Interfaces* **2018**, *10*, 29521–29531.
- (22) Liu, Q.; Jin, J.; Zhang, J. NiCo<sub>2</sub>S<sub>4</sub> @graphene as a Bifunctional Electrocatalyst for Oxygen Reduction and Evolution Reactions. *ACS Appl. Mater. Interfaces* **2013**, *5*, 5002–5008.
- (23) Han, X.; Zhang, W.; Ma, X.; Zhong, C.; Zhao, N.; Hu, W.; Deng, Y. Identifying the Activation of Bimetallic Sites in NiCo<sub>2</sub>S<sub>4</sub>@g-C<sub>3</sub>N<sub>4</sub>-CNT Hybrid Electrocatalysts for Synergistic Oxygen Reduction and Evolution. *Adv. Mater.* **2019**, *31*, 1808281.
- (24) Wang, Y.; Li, X.; Zhang, M.; Zhou, Y.; Rao, D.; Zhong, C.; Zhang, J.; Han, X.; Hu, W.; Zhang, Y.; Zaghib, K.; Wang, Y.; Deng, Y. Lattice-Strain Engineering of Homogeneous NiS<sub>0.5</sub>Se<sub>0.5</sub> Core-Shell Nanostructure as a Highly Efficient and Robust Electrocatalyst for Overall Water Splitting. *Adv. Mater.* **2020**, *32*, 2000231.
- (25) Wang, Y.; Li, X.; Zhang, M.; Zhang, J.; Chen, Z.; Zheng, X.; Tian, Z.; Zhao, N.; Han, X.; Zaghib, K.; Wang, Y.; Deng, Y.; Hu, W. Highly Active and Durable Single-Atom Tungsten-Doped NiS<sub>0.5</sub>Se<sub>0.5</sub> Nanosheet @ NiS<sub>0.5</sub>Se<sub>0.5</sub> Nanorod Heterostructures for Water Splitting. *Adv. Mater.* **2022**, *34*, 2107053.
- (26) Du, J.; Chen, C.; Cheng, F.; Chen, J. Rapid Synthesis and Efficient Electrocatalytic Oxygen Reduction/Evolution Reaction of CoMn<sub>2</sub>O<sub>4</sub> Nanodots Supported on Graphene. *Inorg. Chem.* **2015**, *54*, 5467–5474.
- (27) He, X.; Yin, F.; Li, Y.; Wang, H.; Chen, J.; Wang, Y.; Chen, B. NiMnO<sub>3</sub>/NiMn<sub>2</sub>O<sub>4</sub> Oxides Synthesized via the Aid of Pollen: Ilmenite/Spinel Hybrid Nanoparticles for Highly Efficient Bifunctional Oxygen Electrocatalysis. *ACS Appl. Mater. Interfaces* **2016**, *8*, 26740–26757.
- (28) Kim, T. W.; Woo, M. A.; Regis, M.; Choi, K. S. Electrochemical Synthesis of Spinel Type ZnCo<sub>2</sub>O<sub>4</sub> Electrodes for Use as Oxygen Evolution Reaction Catalysts. *J. Phys. Chem. Lett.* **2014**, *5*, 2370–2374.
- (29) Chakrabarty, S.; Mukherjee, A.; Su, W.-N.; Basu, S. Improved Bi-Functional ORR and OER Catalytic Activity of Reduced Graphene Oxide Supported ZnCo<sub>2</sub>O<sub>4</sub> Microsphere. *Int. J. Hydrogen Energy* **2019**, *44*, 1565–1578.
- (30) Yan, D.; Li, Y.; Huo, J.; Chen, R.; Dai, L.; Wang, S. Defect Chemistry of Nonprecious-Metal Electrocatalysts for Oxygen Reactions. *Adv. Mater.* **2017**, *29*, 1606459.
- (31) Liu, H.; Long, W.; Song, W.; Liu, J.; Wang, F. Tuning the Electronic Bandgap: An Efficient Way To Improve the Electrocatalytic Activity of Carbon-Supported Co<sub>3</sub>O<sub>4</sub> Nanocrystals for Oxygen Reduction Reactions. *Chem.—Eur. J.* **2017**, *23*, 2599–2609.
- (32) Ji, Q.; Bi, L.; Zhang, J.; Cao, H.; Zhao, X. S. The Role of Oxygen Vacancies of ABO<sub>3</sub> Perovskite Oxides in the Oxygen Reduction Reaction. *Energy Environ. Sci.* **2020**, *13*, 1408–1428.
- (33) Wang, H.; Song, X.; Wang, H.; Bi, K.; Liang, C.; Lin, S.; Zhang, R.; Du, Y.; Liu, J.; Fan, D.; Wang, Y.; Lei, M. Synthesis of Hollow Porous ZnCo<sub>2</sub>O<sub>4</sub> Microspheres as High-Performance Oxygen Reduction Reaction Electrocatalyst. *Int. J. Hydrogen Energy* **2016**, *41*, 13024–13031.
- (34) Zhang, J.; Zhang, D.; Yang, Y.; Ma, J.; Cui, S.; Li, Y.; Yuan, B. Facile Synthesis of ZnCo<sub>2</sub>O<sub>4</sub> Mesoporous Structures with Enhanced Electrocatalytic Oxygen Evolution Reaction Properties. *RSC Adv.* **2016**, *6*, 92699–92704.
- (35) Zheng, J.; Xiao, J.; Zhang, J.-G. The Roles of Oxygen Non-Stoichiometry on the Electrochemical Properties of Oxide-Based Cathode Materials. *Nano Today* **2016**, *11*, 678–694.
- (36) Usharani, N. J.; Shringi, R.; Sanghavi, H.; Subramanian, S.; Bhattacharya, S. S. Role of Size, Alio-/Multi-Valecy and Non-Stoichiometry in the Synthesis of Phase-Pure High Entropy Oxide (Co,Cu,Mg,Na,Ni,Zn)O. *Dalton Trans.* **2020**, *49*, 7123–7132.
- (37) Hohenberg, P.; Kohn, W. Inhomogeneous Electron Gas. *Phys. Rev.* **1964**, *136*, B864–B871.
- (38) Kohn, W.; Sham, L. J. Self-Consistent Equations Including Exchange and Correlation Effects. *Phys. Rev.* **1965**, *140*, A1133–A1138.
- (39) Kresse, G.; Hafner, J. Ab Initio Molecular Dynamics for Liquid Metals. *Phys. Rev. B: Condens. Matter Mater. Phys.* **1993**, *47*, 558–561.
- (40) Kresse, G.; Furthmüller, J. Efficient Iterative Schemes for Ab Initio Total-Energy Calculations Using a Plane-Wave Basis Set. *Phys. Rev. B: Condens. Matter Mater. Phys.* **1996**, *54*, 11169–11186.
- (41) Kresse, G.; Joubert, D. From Ultrasoft Pseudopotentials to the Projector Augmented-Wave Method. *Phys. Rev. B: Condens. Matter Mater. Phys.* **1999**, *59*, 1758–1775.
- (42) Anisimov, V. I.; Zaanen, J.; Andersen, O. K. Band Theory and Mott Insulators: Hubbard U Instead of Stoner I. *Phys. Rev. B: Condens. Matter Mater. Phys.* **1991**, *44*, 943–954.
- (43) Dudarev, S. L.; Botton, G. A.; Savrasov, S. Y.; Humphreys, C. J.; Sutton, A. P. Electron-Energy-Loss Spectra and the Structural Stability of Nickel Oxide: An LSDA+U Study. *Phys. Rev. B: Condens. Matter Mater. Phys.* **1998**, *57*, 1505–1509.
- (44) Sun, J.; Ruzsinszky, A.; Perdew, J. P. Strongly Constrained and Appropriately Normed Semilocal Density Functional. *Phys. Rev. Lett.* **2015**, *115*, 036402.
- (45) Gautam, G. S.; Carter, E. A. Evaluating Transition Metal Oxides within DFT-SCAN and SCAN+U Frameworks for Solar Thermochemical Applications. *Phys. Rev. Mater.* **2018**, *2*, 095401.
- (46) Long, O. Y.; Gautam, G. S.; Carter, E. A. Evaluating Optimal U for 3d Transition-Metal Oxides within the SCAN+U Framework. *Phys. Rev. Mater.* **2020**, *4*, 045401.
- (47) Hellenbrandt, M. The Inorganic Crystal Structure Database (ICSD)—Present and Future. *Crystallogr. Rev.* **2004**, *10*, 17–22.
- (48) Ong, S. P.; Richards, W. D.; Jain, A.; Hautier, G.; Kocher, M.; Cholia, S.; Gunter, D.; Chevrier, V. L.; Persson, K. A.; Ceder, G. Python Materials Genomics (Pymatgen): A Robust, Open-Source Python Library for Materials Analysis. *Comput. Mater. Sci.* **2013**, *68*, 314–319.
- (49) Hanawalt, J. D.; Rinn, H. W.; Frevel, L. K. Chemical Analysis by X-Ray Diffraction. *Ind. Eng. Chem.* **1938**, *10*, 457–512.

- (50) Dillip, G. R.; Banerjee, A. N.; Joo, S. W. Conductivity Inversion of ZnO Nanoparticles in ZnO-Carbon Nanofiber Hybrid Thin Film Devices by Surfactant-Assisted C-Doping and Non-Rectifying, Non-Linear Electrical Properties via Interfacial Trap-Induced Tunneling for Stress-Grading Applications. *J. Appl. Phys.* **2019**, *125*, 175106.
- (51) Oriani, R. A. Ostwald Ripening of Precipitates in Solid Matrices. *Acta Metall.* **1964**, *12*, 1399–1409.
- (52) Wang, Z.; Lu, S.; He, G.; Lv, A.; Shen, Y.; Xu, W. In Situ Construction of Dual-Morphology  $\text{ZnCo}_2\text{O}_4$  for High-Performance Asymmetric Supercapacitors. *Nanoscale Adv.* **2019**, *1*, 3086–3094.
- (53) Dillip, G. R.; Banerjee, A. N.; Anitha, V. C.; Joo, S. W.; Min, B. K.; Sawant, S. Y.; Cho, M. H. Anchoring Mechanism of ZnO Nanoparticles on Graphitic Carbon Nanofiber Surfaces through a Modified Co-Precipitation Method to Improve Interfacial Contact and Photocatalytic Performance. *ChemPhysChem* **2015**, *16*, 3214–3232.
- (54) Ma, Y.; Yang, Y.; Dai, X.; Luan, X.; Yong, J.; Qiao, H.; Zhao, H.; Cui, M.; Zhang, X.; Huang, X. Simultaneous Modulation of Composition and Oxygen Vacancies on Hierarchical  $\text{ZnCo}_2\text{O}_4/\text{Co}_3\text{O}_4$ /NC-CNT Mesoporous Dodecahedron for Enhanced Oxygen Evolution Reaction. *Chem.—Eur. J.* **2018**, *24*, 18689–18695.
- (55) Gutturu, R. R.; Rajavaram, R.; Borelli, D. P. R. Effect of Reaction Time and PVP Contents on Morphologies of Hierarchical 3D Flower-like  $\text{ZnCo}_2\text{O}_4$  Microstructures for Energy Storage Devices. *Int. J. Energy Res.* **2020**, *44*, 11233–11247.
- (56) Xu, N.; Nie, Q.; Liu, J.; Huang, H.; Qiao, J.; Zhou, X.-D. Insert  $\text{Zn}^{2+}$  in Tetrahedral Sites of Bi-Metal Zn-Co Spinel Oxides with High Oxygen Catalytic Performance for Liquid and Flexible Zinc-Air Batteries. *J. Electrochem. Soc.* **2020**, *167*, 050512.
- (57) Mandal, B.; Roy, P.; Mitra, P. Comparative Study on Organic Effluent Degradation Capabilities and Electrical Transport Properties of Polygonal  $\text{ZnCo}_2\text{O}_4$  Spinels Fabricated Using Different Green Fuels. *Mater. Sci. Eng. C* **2020**, *117*, 111304.
- (58) Liu, Z.; Cheng, H.; Li, N.; Ma, T. Y.; Su, Y.  $\text{ZnCo}_2\text{O}_4$  Quantum Dots Anchored on Nitrogen-Doped Carbon Nanotubes as Reversible Oxygen Reduction/Evolution Electrocatalysts. *Adv. Mater.* **2016**, *28*, 3777–3784.
- (59) Liu, J.; Bao, H.; Zhang, B.; Hua, Q.; Shang, M.; Wang, J.; Jiang, L. Geometric Occupancy and Oxidation State Requirements of Cations in Cobalt Oxides for Oxygen Reduction Reaction. *ACS Appl. Mater. Interfaces* **2019**, *11*, 12525–12534.
- (60) Sreekanth, T. V. M.; Nagajyothi, P. C.; Devarayapalli, K. C.; Shim, J.; Yoo, K. Lilac Flower-Shaped  $\text{ZnCo}_2\text{O}_4$  Electrocatalyst for Efficient Methanol Oxidation and Oxygen Reduction Reactions in an Alkaline Medium. *CrystEngComm* **2020**, *22*, 2849–2858.
- (61) Bao, J.; Wang, Z.; Liu, W.; Xu, L.; Lei, F.; Xie, J.; Zhao, Y.; Huang, Y.; Guan, M.; Li, H.  $\text{ZnCo}_2\text{O}_4$  ultrathin nanosheets towards the high performance of flexible supercapacitors and bifunctional electrocatalysis. *J. Alloys Compd.* **2018**, *764*, 565–573.
- (62) Deeloed, W.; Priamushko, T.; Cizek, J.; Suramitr, S.; Kleitz, F. Defect-Engineered Hydroxylated Mesoporous Spinel Oxides as Bifunctional Electrocatalysts for Oxygen Reduction and Evolution Reactions. *ACS Appl. Mater. Interfaces* **2022**, *14*, 23307–23321.

## □ Recommended by ACS

### Highly Efficient and Stable Bifunctional Electrocatalyst with Alloy/Oxide Heterostructures for a Rechargeable Zinc-Air Battery

Chang Rui, Yunfei Bu, et al.

OCTOBER 02, 2022

ENERGY & FUELS

READ ▶

### Facile Synthesis of Schlumbergera Bridgesii-Like Nanostructured $\text{Co}_3\text{O}_4@\text{MnO}_2$ as High Performance Electrode Materials for Supercapacitors

Qian Wang, Zhihao Zhang, et al.

NOVEMBER 23, 2022

INDUSTRIAL & ENGINEERING CHEMISTRY RESEARCH

READ ▶

### Hierarchical Hollow $\text{CoWO}_4-\text{Co(OH)}_2$ Heterostructured Nanoboxes Enabling Efficient Water Oxidation Electrocatalysis

Hui Xu, Yukou Du, et al.

AUGUST 24, 2022

INORGANIC CHEMISTRY

READ ▶

### In Situ Grown Cuboidal $\text{MnCo}_2\text{O}_4/\text{h}$ Boron Nitride Heterojunction: A Noble Metal-Free Approach Based on Efficient Hole Extraction for Electrochemical Oxygen Evo...

Adit Kumar Shah and Mohammad Qureshi

JANUARY 15, 2022

ACS APPLIED ENERGY MATERIALS

READ ▶

Get More Suggestions >